AIAA JOURNAL
Vol. 46, No. 3, March 2008

Stability of Vortex Pairs over Slender Conical Bodies: Analysis and Numerical Computation

Jinsheng Cai* and Her-Mann Tsai†
Temasek Laboratories, National University of Singapore, Singapore, 119260 Republic of Singapore
and
Shijun Luo‡ and Feng Liu§
University of California, Irvine, California 92697-3975

DOI: 10.2514/1.33498

Analytical studies and computational fluid dynamics simulations are presented to study the formation and stability of stationary symmetric and asymmetric vortex pairs over slender conical bodies in an inviscid incompressible flow at high angles of attack. The analytical method is based on an eigenvalue analysis on the motion of the vortices under small perturbations. A three-dimensional time-accurate Euler code is used to compute five typical flows studied by the analytical method on extraordinarily fine grids with strict convergence criteria. Both the theory and the computation show that the vortices over a delta wing are stable and those over a wing–body configuration at the low angle of attack are symmetric and stable, but become asymmetric and bistable at higher angles of attack; that is, the vortices shift to one of two stable mirror-imaged asymmetric configurations. The computational results agree well with the analytical predictions, demonstrating the existence of a global inviscid hydrodynamic instability mechanism responsible for the asymmetry of separation vortices over slender conical bodies.

I. Introduction

AN INITIALLY symmetric vortex pair over a slender pointed body or wing–body combination, such as that shown in Fig. 1, becomes asymmetric as the angle of attack is increased beyond a certain value, causing large rolling moments in the case of swept wings or large side forces in the case of slender bodies, even at zero roll and yawing angles. At even larger angles of attack, unsteady vortex shedding will appear. Because of the difficult nature of the problem, the mechanism of the breaking of symmetry of such vortex flows is not clear. A great deal of disagreement has been developed regarding the understanding, prediction, and control of the vortex asymmetry, despite much experimental, theoretical, and computational effort spent on the topic. The subject has been reviewed by Hunt [1], Ericsson and Reding [2], and Champigny [3].

It is found by many experimental observations [4–6] and numerical studies [7–10] that a microscale asymmetric perturbation close to the nose tip produces a strong flow asymmetry at high angles of attack. There seems to be little doubt that the vortex asymmetry is triggered, formed, and developed in the apex region. Because the apex portion of any slender pointed body is nearly a conical body, high-angle-of-attack flow about conical bodies has been studied analytically. Using the separation-vortex flow model of Bryson [11], Dyer et al. [12] found that in addition to stationary symmetric vortex-flow solutions, there exist stationary asymmetric vortex-flow solutions over circular cones when the angle of attack is larger than about twice of the semivertex angle, even though the separation lines are postulated at symmetric positions. The stability of these stationary vortices were investigated analytically by Pidd and Smith [13]. Two types of instability may be classified. The absolute-type instability refers to situations in which a perturbation initially introduced at a given spatial point grows both upstream and downstream, resulting in a global change of the flowfield even after the initial perturbation is withdrawn. The convective type, on the other hand, refers to conditions in which the initial perturbation grows only in the downstream direction of the flow, and thus the flow returns to its original state after the disturbances caused by the initial perturbation are convected out of the domain on the withdrawal of the initial perturbation. Pidd and Smith [13] introduced a small change in the positions of the originally stationary symmetric/asymmetric conical vortices into the flow near the body tip. Under the assumptions of the slender-body theory, they studied the growth of such disturbances in the downstream direction. They showed that the stationary symmetric vortex pairs were convectively stable in a narrow band of values of the incidence parameter, whereas the stationary asymmetric vortex pairs are convectively stable, with insignificant exceptions.

Degani [7,8] and Levy et al. [9] studied the separation vortices over a 3.5-caliber tangent-ogive-cylinder body of revolution at low speeds by numerical computations using a time-accurate Navier–Stokes method. They found that it is necessary to maintain a fixed small geometric disturbance near the body apex to obtain and keep an asymmetric vortex pattern from the originally symmetric vortex pattern in their numerical computations. This finding in numerical computation coupled with an experimental observation of Degani and Tobak [14] led them to believe that a convective instability mechanism was responsible for the onset of asymmetry of the otherwise symmetric vortices over a slender body of revolution with a pointed nose.

In a separate numerical study, however, Hartwich et al. [10] reported an asymmetric vortex-flow solution of the incompressible three-dimensional turbulent Navier–Stokes equations for a 3.5-caliber tangent-ogive cylinder at an angle of attack of 40 deg without the imposition of a fixed geometric asymmetry in the computations. It was claimed that the asymmetric solution is triggered by computer round-off errors in the computations. This finding suggests an absolute or global instability mechanism. In addition, there are experimental observations that support such a mechanism (for example, the existence of a bistable variation of leeside flowfield

Received 17 July 2007; revision received 30 October 2007; accepted for publication 1 November 2007.

*Research Scientist, Kent Ridge Crescent. Member AIAA.
†Principal Research Scientist, Kent Ridge Crescent. Member AIAA.
‡Researcher, Department of Mechanical and Aerospace Engineering.
§Professor, Department of Mechanical and Aerospace Engineering. Associate Fellow AIAA.

with roll angle of ogive cylinders at incidence angles in the range of 50–60 deg [4,6]) and the hysteresis effects detected in experiments in which asymmetric vortex-flow patterns over slender bodies of revolution were mirror-imaged by applying suction or blowing [15,16].

Using the simplified separation-vortex-flow model of Legendre [17], Huang and Chow [18] succeeded in showing analytically that the vortex pair over a slender flat-plate delta wing at zero sideslip can be stationary and is stable under small conical perturbations. Using the same flow model, Cai et al. [19] developed a stability theory for stationary conical vortex pairs over general slender conical bodies under the assumption of conical flow and classical slender-body theory. Cai et al. extended the method described in [19] to study the stability of a stationary asymmetric vortex pair over slender conical bodies and wing–body combinations with and without sideslip [20,21].

In this paper, a time-accurate three-dimensional Euler code is used to validate and confirm the stability analysis of Cai et al. [20,21]. Complete three-dimensional flows at typical flow conditions that vary from stable to unstable regimes as determined by the stability analysis in [20,21] are computed by an Euler flow solver. Stationary vortex configurations are first captured by running the Euler code in its steady-state mode until the residual in the continuity equation is reduced by more than 11 orders of magnitude, starting from the uniform freestream condition. After a stationary-vortex-flow configuration is obtained, a transient asymmetric perturbation consisting of suction and blowing of short duration on the left- and right-hand sides of the wing is introduced to the flow and the Euler code is run in time-accurate mode to determine if the flow will return to its original undisturbed condition or evolve into a different steady or unsteady solution. The former case indicates that the original stationary vortex configuration is stable to the applied perturbations, whereas the latter case proves it unstable or neutrally stable if the flow would continue oscillating around the original stationary solution. Strict conical bodies are studied to avoid confusion with other types of axisymmetric but nonconical slender bodies.

Euler computations are used in this study, partially to avoid the added computational cost and uncertainties with turbulence modeling associated with Navier–Stokes computations and, more important, because the analytical work in [20,21] is based on inviscid theory. It is then natural to perform Euler computations to investigate the inviscid mechanisms of the vortex dynamics in the theory. Viscosity plays a critical role in determining the location of separation and any potential appearance of secondary vortices, which the Euler model in general cannot accurately resolve. The present study is restricted to bodies with sharp leading edges so that the uncertainty of the location of flow separation is removed in the Euler computations. Viscous effects also dictate the structure of the vortex core. However, these effects are believed to have secondary importance on the vortex dynamics of the concentrated vortex pairs. In addition, [22] presented evidence that even an Euler model may yield vortex-core structures that closely resemble experimental measurement.

It must be pointed out that vortices over a forebody may also lose stability and symmetry due to vortex breakdown, which is certainly beyond the scope of the present study. However, vortex breakdown usually happens at very large angles of attack or farther downstream of the body. Many experimental and computational studies show that vortex asymmetry very often occurs before vortex breakdown.

In the following sections, the basic theory and typical analytical results are summarized. The numerical method is then described and used to compute the stationary vortex flowfields and study their stability under small temporal perturbations of suction and blowing for five typical cases selected from the analytical studies. The computational results are compared with the analytical predictions and then conclusions are drawn.

II. Theoretical Analysis

In this section, the vortex model and the stability analysis developed in Cai et al. [19–21] are summarized. Consider the flow

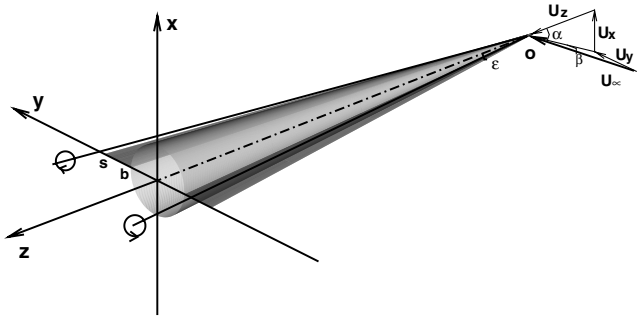

Fig. 1 Slender conical wing–body combination and separation vortices.

past a slender conical wing–body combination at an angle of attack α and sideslip angle β, as shown in Fig. 1. The velocity of the freestream flow is U_∞. The combination has a slender triangular flat-plate wing passing through the longitudinal axis of a cone body. The flat-plate wing has a half-vertex angle of ϵ. In a cross-sectional plane at z, the wing has a half-span s, and the centerbody has a half-width b. The wing–body combination is assumed to be conical and of infinite length. No effects of the trailing edge or body base are considered. At high angles of attack, a pair of symmetric or asymmetric vortices appear on the back of this wing–body combination, depending on the flow conditions and the wing–body geometry. Slight perturbations in the flow may or may not cause large deviations of the vortex configuration. Stability in the present study is defined as the ability of the vortices to return to their original configuration on application and subsequent withdrawal of small disturbances introduced to the flow, often referred to as the absolute type of stability.

Based on the available experimental observations, the vortex model chosen here consists of one pair of concentrated vortices separated from the leading edge of the flat-plate wing, as shown in Fig. 1. The distributed vortex sheets that connect the leading edges and the two concentrated vortices are neglected because their strength is, in general, much smaller than that of the two concentrated vortices. The two concentrated vortices are assumed to be conical rays from the body apex O. Secondary separation vortices, if any, are weak and are thus also neglected. Vortex breakdown is not considered. The flow is assumed to be steady, inviscid, incompressible, conical, and slender. The flow is irrotational, except at the center of the isolated vortices.

By using the assumption of slender and conical flow, Cai et al. [19–21] were able to reduce the three-dimensional flow problem to a two-dimensional flow problem. For the simple cross-sectional profile shown in Fig. 1, the solution for the two-dimensional problem can be found by a conformal mapping $\zeta = \zeta(Z)$ that maps the body contour in the plane $Z = x + iy$ to a circle of radius r in an uniform flow of velocity $(U_x/2, U_y/2)$ in the plane $\zeta = \xi + i\eta$, in which $U_x = U_\infty \cos\beta \sin\alpha$ and $U_y = U_\infty \sin\beta$. In addition, the condition of conical flow in which the flow is invariant along rays emanating from the apex is implemented to obtain the solution of the flow induced by the axial component of the freestream velocity, $U_z = U_\infty \cos\beta \cos\alpha$. Let Z_1 (or ζ_1 on the transformed plane) be the location of the first vortex. Cai et al. [20] gave the complex velocity at Z_1 as follows.

$$u_1 - iv_1 = \left[\frac{1}{2}\left(\bar{U}_n - \frac{U_n r^2}{\zeta_1^2}\right) + \frac{i\Gamma_1}{2\pi}\left(-\frac{1}{\zeta_1 - r^2/\bar{\zeta}_1}\right) - \frac{i\Gamma_2}{2\pi}\left(\frac{1}{\zeta_1 - \zeta_2} - \frac{1}{\zeta_1 - r^2/\bar{\zeta}_2}\right)\right]\left(\frac{\mathrm{d}\zeta}{\mathrm{d}Z}\right)_1 - \frac{i\Gamma_1}{4\pi}\left(\frac{\mathrm{d}^2 Z}{\mathrm{d}\zeta^2}\right)_1\left(\frac{\mathrm{d}\zeta}{\mathrm{d}Z}\right)_1^2 - \frac{U_x \bar{Z}_1}{sK} + \frac{1}{2\pi}\sum_{j=1}^{N}\frac{Q_j}{Z_1 - Z_j} \tag{1}$$

where $U_n = U_x(1 + iK_S)$, $K = \tan\alpha/\tan\epsilon$ is the Sychev similarity parameter [23], $K_S = \tan\beta/\sin\alpha$ is the sideslip similarity parameter, $Q_j (j = 1, 2, \ldots, N)$ are the strengths of the point sources

to be determined by N simultaneous equations of the boundary conditions at the points Z_j on the body contour, and the subscript 1 denotes the values at vortex point Z_1 (or $\zeta = \zeta_1$). A similar expression is obtained for the complex velocity at the center of the other vortex denoted by Z_2 (or ζ_2).

Only vortex configurations (locations and strengths of the vortices) that result in zero flow velocities at the two vortex centers can exist in a steady flow. These locations of the vortices are called the *stationary* positions. The stationary positions Z_1 and Z_2 and strengths Γ_1 and Γ_2 of the two vortices in the preceding model are determined by solving a set of four algebraic equations by a Newton iteration method [20]. Among the four equations, two equations set the vortex velocities to zero, and the other two equations set the flow velocities at the separation points to zero or finite.

When a vortex pair is slightly perturbed from its stationary position and then released, its motion follows the vortex velocity. After linearization, the increments of its coordinates as functions of time are governed by a system of two linear, homogeneous, first-order, ordinary differential equations. Define the Jacobian and divergence of the vortex velocity field $\boldsymbol{q} = (u, v)$.

$$J = \begin{vmatrix} \frac{\partial u}{\partial x} & \frac{\partial u}{\partial y} \\ \frac{\partial v}{\partial x} & \frac{\partial v}{\partial y} \end{vmatrix}, \qquad D = \nabla \cdot \boldsymbol{q} = \frac{\partial u}{\partial x} + \frac{\partial v}{\partial y} \tag{2}$$

It is shown [19] that the eigenvalues of this problem are

$$\lambda_{1,2} = \tfrac{1}{2}\left(D_0 \pm \sqrt{D_0^2 - 4J_0}\right) \tag{3}$$

where the subscript 0 denotes values at the stationary position of the considered vortex.

The eigenvalues λ_1 and λ_2 depend on the Sychev similarity parameter K, the sideslip similarity parameter K_S, and other geometric parameters such as the body–wing span ratio $\gamma = b/s$. Any perturbation of the stationary positions of the vortex pair can be decomposed into a symmetric perturbation and an antisymmetric perturbation. The maximum real part of the two eigenvalues λ_1 and λ_2 for each vortex of the stationary vortex pair under small symmetric or antisymmetric perturbations is used to determine stability in this analysis. A positive value of this variable means growth of the perturbation (unstable), a negative value means decay of the perturbation (stable), and a zero value means that the perturbation persists with constant amplitude (neutrally stable). A vortex pair is stable if and only if both vortices are stable under both symmetric and antisymmetric perturbations.

III. Numerical Method

A. Three-Dimensional Time-Accurate Euler Solver

To verify the preceding theoretical analysis, a three-dimensional time-accurate Euler solver is used to compute the separation-vortex flows over slender conical bodies studied by the analytical method. The present solver is based on a parallel, multiblock, multigrid, finite volume method for the steady and unsteady Euler equations. The method uses a second-order central-difference scheme for spatial discretization with fourth-order artificial dissipation. Unsteady time-accurate computations are achieved by using a second-order-accurate implicit scheme with dual time stepping. An explicit Runge–Kutta-type scheme is used to perform the time marching in pseudotime. The resulting code preserves symmetry. The multiblock solver has been validated for a number of steady and unsteady cases [24–27]. An extension of the code to include blocks with nonmatching grid points and also general overset grids is implemented and validated in [28]. To maintain a fine grid in areas of high vorticity and reduce computation in the far field, nonoverlapping blocked grids with unmatched grid points are sometimes used. The grid points across such block boundaries are not matched only in the circular circumferential direction. Therefore, an accurate one-dimensional flux-matching interpolation scheme can be used. Notice also that such block boundaries are used only in the far-field region away from the vortices.

It is noted that computation of the stability behavior of the separation vortices is a rather difficult task. As Cummings et al. [29] pointed out,

> Although some researchers are content to allow the algorithm to supply the perturbation that must be there anyway (from a physical perspective), it is much more desirable to use an algorithm that does not add an unknown level of perturbation. It would be superior to have the perturbation be added explicitly as a geometric disturbance or flowfield disturbance.

Levy et al. [30] showed that inherent biases contained in a numerical algorithm generate anomalous asymmetries in the flow. To perform numerical studies of vortex-flow stability, the numerical algorithm is required to be symmetric to obtain the basic symmetric vortex-flow solutions when the boundary and initial conditions are perfectly symmetric. Flows at high angles of attack are especially sensitive to artificial viscosity or numerical dissipation. Hartwich [31] demonstrated that excessive numerical dissipation due to a first-order-accurate difference scheme in the exit boundary condition suppresses symmetry breaking. In his Navier–Stokes computations of a supersonic viscous flow over a 5-deg half-angle cone at an angle of attack of 20 deg, Thomas [32] found that an inadequate grid resolution near the body tip gives rise to a spurious asymmetry. In an Euler computation, high gradients exist in the regions of shear-layer separation and the vortex cores, in addition to areas in the vicinity of the body surface. Appropriate grid topology with sufficient grid density in these regions is vital to the present study.

Special attention is given to the preceding issues in the present study. In particular, care is taken to make sure that we impose perfectly symmetric initial and boundary conditions on sufficiently fine and perfectly symmetric grids. The central-differencing scheme with fourth-order artificial dissipation guarantees the needed algorithmic symmetry in space. Because an explicit time-marching scheme is used to integrate in time, inherent biases introduced in the time marching, such as that found in the diagonal algorithm revealed by Levy et al. [30], are not present in our computations. These measures ensure that we obtain symmetric base flow solutions in our numerical stability studies.

B. Validation of the Conical-Flow Assumption

It is known that a subsonic flow over a conical body cannot be strictly conical. However, if the conical body is slender, the flow is nearly conical. This was observed in water tunnel for a triangular thin wing of $\epsilon = 15$ deg at $\alpha = 20$ deg and the Reynolds number 20,000 based on chord by Werlé in 1961, as shown in [33], and also demonstrated by Navier–Stokes computations of, for example, Thomas et al. [34]. To examine how good the conical-flow assumption is for the slender conical bodies under present consideration, a numerical experiment is performed with the Euler method. The steady flow about a flat-plate delta wing of $\epsilon = 8$ deg at $\alpha = 20$ deg and $M_\infty = 0.1$ is calculated by the three-dimensional Euler solver in steady-state mode.

Figures 2a and 2b show the computational grid in the incidence and exit planes, respectively. Only every other line is shown in the radial and circumferential directions, for clarity. A strict conical body is of infinite length. However, our computation will have to be restricted to a finite length of the body. The upstream boundary of the computational domain is taken to be one body length away from the vertex of the body. The downstream exit boundary of the computational domain consists of a circular plane with a radius of $25S$, in which S is the half-span of the wing at the exit-flow cross section. For the purpose of validating the assumption of conical flow, we can restrict ourselves to symmetric vortex flows without loss of generality. Consequently, only half-space is computed. The grid in the half-space consists of $25 \times 145 \times 225$ grid points in the longitudinal (along the conical rays), radial, and circumferential directions, respectively. It is a multiblock grid with eight blocks of different grid densities to match the flow gradients and facilitate parallel processing. This grid is significantly finer in the radial and circumferential directions than the $59 \times 50 \times 120$ and $40 \times 65 \times$

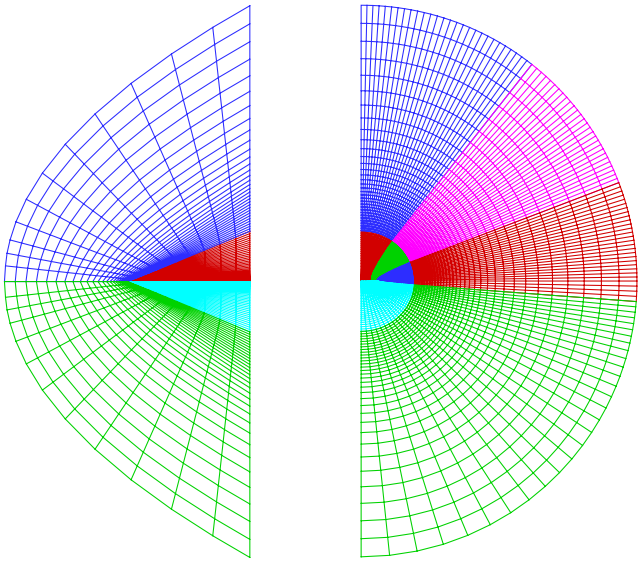

a) b)

Fig. 2 Grid for a flat-plate delta wing: a) incidence plane and b) exit plane.

145 grids used by Degani [7] and Hartwich et al. [10], respectively, in their full-space Navier–Stokes computations of ogive-cylinder bodies. The grid used here also has higher transverse density than the $81 \times 49 \times 161$ grid used by Rizzi [35] for a half-space of the 70-deg swept Dillner wing at $\alpha = 15$ deg and $M_\infty = 0.7$.

The freestream Mach number is set at 0.1 to approximate an incompressible flow for all computations reported in the present paper. A zero-normal-velocity boundary condition is applied on the wing surface. The Kutta condition at the sharp leading edges of the wing is satisfied automatically in an Euler code. Characteristics-based conditions are used on the upstream boundary of the grid. On the downstream boundary, all flow variables are extrapolated to reflect an infinitely long conical body. The conventional method of specifying a back pressure is not applicable for this purpose. No numerical problems are observed in our computations with this outflow boundary condition.

Computations are performed starting from a uniform freestream flow until the maximum residual of the continuity equation is reduced by more than 11 orders of magnitude. Such a stringent convergence criterion is needed for stability studies of high angle-of-attack flows, as is pointed out by Siclari and Marconi [36].

Figure 3 shows the contours of constant pressure in the flowfield. The static pressure decreases to a minimum toward the center of the high-vorticity region, which is taken as the vortex core. The contours consist of conical rays, except near the wing vertex, indicating that

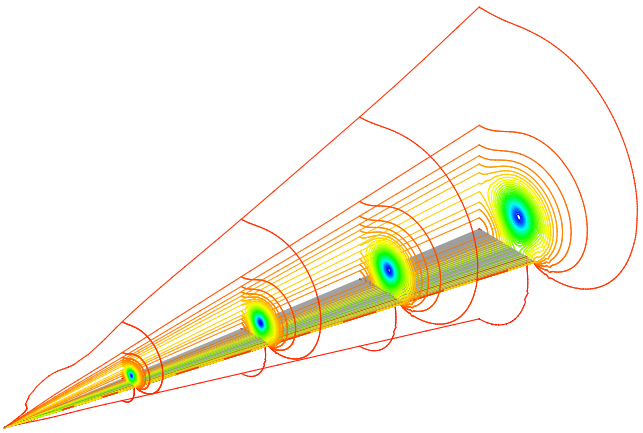

Fig. 3 Pressure contours over a flat-plate delta wing; $\epsilon = 8$ deg and $\alpha = 20$ deg.

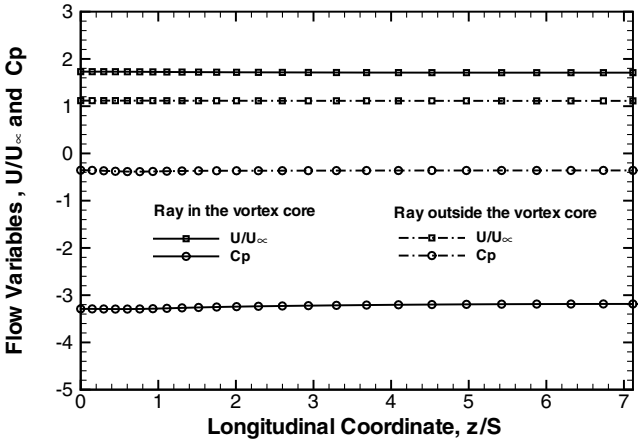

Fig. 4 Variation of flow parameters along rays over a flat-plate delta wing; $\epsilon = 8$ deg and $\alpha = 20$ deg.

the flowfield is practically conical over most of the wing (i.e., quantities being constant along rays from the apex).

To examine this in more detail, Fig. 4 plots the pressure coefficient C_p and the total velocity U/U_∞ along the ray in the vortex core at $(x/s, y/s) = (0.4654, 0.7013)$ and another outside of the vortex core at $(x/s, y/s) = (1.2495, 1.5939)$. The variations of the two flow quantities are nearly negligible. Therefore, we can say that the conical-flow assumption is a good approximation.

In principle, a conical flow can be solved in a two-dimensional plane with the appropriate modified equations. However, the present studies maintain the use of a three-dimensional code on a three-dimensional conical grid to allow calculation of nonconical flows. For the nearly conical flows studied in the present paper, the grid used in the preceding computations is replaced by a conical grid. Figure 5a gives the grid on the incidence plane, and Fig. 5b shows the grid on the right-hand half of the exit plane, although a full cross-plane grid is used in the following computations. Only every other line is shown in the radial and circumferential directions, for clarity. The original lateral boundary is replaced by a cone surface that shares the same apex with the conical body. This cone surface is $25s$ distance away from the body axis at each cross section normal to the body axis,

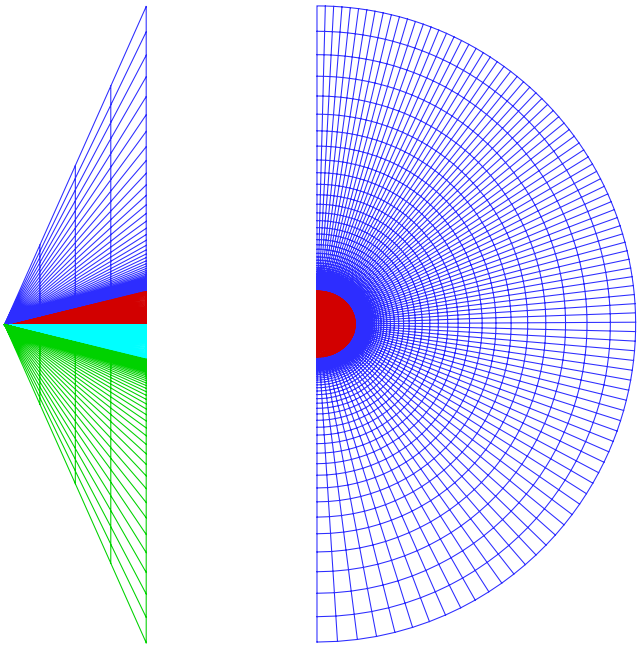

a) b)

Fig. 5 Conical grid for a flat-plate delta : a) incidence plane and b) right-half exit plane.

where s is the local wing semispan. Far-field boundary conditions are applied on this lateral conical boundary. Grids are bunched into one point at the body apex. No numerical difficulties are encountered at the vertex point, because a cell-centered finite volume method is used. Only a few grid lines are needed in the longitudinal direction for conical-flow calculations, and five longitudinal grid lines are chosen for the following computations. However, very fine grids in the radial and circumferential directions in the cross planes must be used to resolve the vortical flowfield for the purpose of stability studies. To investigate flow asymmetry, the full crossflow plane must be included. Grid refinement studies were performed and show that coarser grids yield significant position shifts of the stationary vortex cores and could lead to erroneous prediction of the stability of the vortex flow. The grid densities used for the calculations presented in the following sections represent those determined based on the grid refinement studies and a balance of available computing resources.

C. Temporal Perturbations

Small temporal perturbations through the use of suction and blowing are introduced to a converged vortex-flow solution to study its stability. Suction and blowing slots consist of narrow conical regions on the upper surfaces of the wing. The two slots are symmetric to the incidence plane and located approximately beneath the vortex cores. The perturbations are activated in the initial time period $0 < t < 1$ of the time-accurate Euler computation, where t is a nondimensional time. The air-blowing velocity V_j is a function of y/s and t. On the right-hand side of the wing, looking toward the downstream direction,

$$V_j = \begin{cases} V_0 \sin\left(\frac{y-y_1}{y_2-y_1}\pi\right) \sin(\pi t), & 0 \le t \le 1, y_1 \le y \le y_2 \\ 0, & \text{otherwise} \end{cases} \quad (4)$$

The same expression of Eq. (4) holds for the slot on the left-hand side of the wing, except with a negative sign in front of V_0 to obtain an antisymmetric perturbation. Antisymmetric perturbations are used because they are found to be the most unstable modes of motion in the theory [19]. Three configurations of antisymmetric perturbations are used by choosing different values of the parameters in Eq. (4). Perturbation A has $y_1 = 0.45s$, $y_2 = 0.60s$, and $V_0 = 2.0U_\infty$; perturbation B has $y_1 = 0.73s$, $y_2 = 0.78s$, and $V_0 = 2.0U_\infty$; and perturbation C has $y_1 = 0.90s$, $y_2 = 0.95s$, and $V_0 = -1.33U_\infty$. The instantaneous maximum blowing momentum flux occurs at $t = 1/2$. The instantaneous maximum blowing momentum-flux coefficient based on the wing area c_μ is 0.3, 0.1, and 0.04, respectively. The corresponding air-blowing force is about one order of magnitude less than the normal force acting on the body. The suction and blowing are simulated in the computations by enforcing outward normal velocities equal to the specified V_j at the blowing/suction slots.

Within the regime of linear stability, the nature of stability does not depend on the size of the initial disturbance. However, the time to a noticeable disturbance depends on the initial amplitude of the disturbance. In addition, it is noted that perturbations of the vortex positions can be directly imposed in the mathematical theory. In the computations, however, it takes time for the velocity perturbations on the body surface to reach the vortex-core locations. Different initial perturbations are tested in our computations. For a stable configuration, the vortex locations return to their original positions very quickly when the initial perturbations are small. For unstable configurations, it takes too long for the disturbances to grow to a clearly noticeable level. The particular levels of suction and blowing already specified are used to obtain the distinctly discernible trajectories of the vortices and also to do so within a finite computational time. Obviously, if a vortex configuration is stable under relatively large perturbations, it must be stable for smaller perturbations. For an unstable configuration, the minimum perturbation needed to demonstrate instability in a computation depends on the computational resources (in terms of both computer time and memory.) Theoretically, there is no such a minimum. The smaller the initial disturbance, the longer the time needed for the disturbance to develop and the finer the computational mesh that must be used to reduce numerical dissipation, which exists in any computational method. Both factors cause undue increases of the computational time and memory.

IV. Flat-Plate Delta Wing with and Without Sideslip

Stationary vortex configurations and their stability can be determined by the theory presented in Sec. II. Reference [19] discusses the case without sideslip ($K_S = 0$) in detail. Symmetric vortex pairs are found over flat-plate delta wings for a range of angles of attack or in terms of the similarity parameter K. Reference [20] further shows that there are no asymmetric stationary vortices at zero sideslip. Figure 6 plots the maximum real part of the eigenvalues λ_1 and λ_2 of the vortex motion for the stationary symmetric vortex pairs vs the similarity parameter K. The eigenvalues remain negative for the whole range of K considered. This indicates that the symmetric vortex pair over the flat-plate delta wing is stable for all angles of attack.

With sideslip, the stationary vortex pair becomes asymmetric [20]. Relative to the stationary symmetric vortex pair, the windward vortex moves inboard and remains nearly the same distance above the upper surface of the wing, whereas the leeward vortex moves outboard and upward from the wing. Figure 7 gives the maximum real part of the eigenvalues λ_1 and λ_2 of the vortex motion under small symmetric and antisymmetric disturbances against the Sychev similarity parameter K for the sideslip similarity parameter $K_S = 0.5$. The maximum real part of the eigenvalues is negative for all the cases considered.

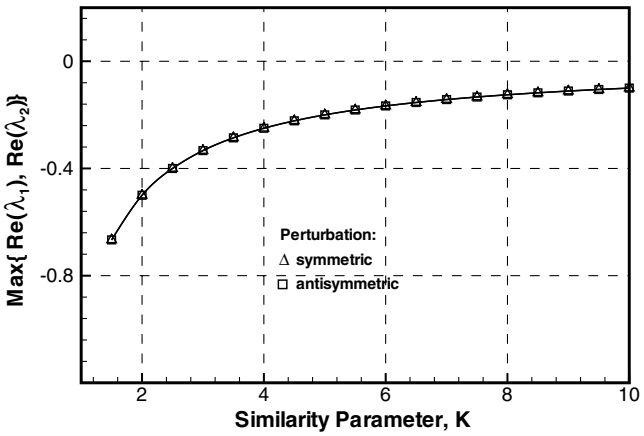

Fig. 6 Maximum real part of eigenvalues vs K for symmetric vortex pairs over a flat-plate delta wing at zero sideslip.

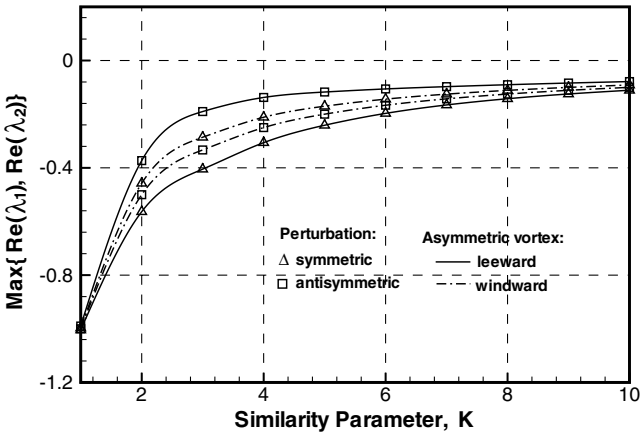

Fig. 7 Maximum real part of eigenvalues of asymmetric vortex pairs over a flat-plate delta wing vs K; $K_S = 0.5$.

To computationally verify the preceding analytical predictions, the time-accurate three-dimensional Euler code already described is used to study two particular flight conditions for the flat-plate delta wing of $\epsilon = 8$ deg: a symmetric case with zero sideslip ($\beta = 0$ deg) and an asymmetric case with nonzero sideslip ($\beta = 13$ deg), both at an angle of attack of 28 deg corresponding to $K = 3.7833$. The corresponding sideslip similarity parameter K_S is 0 and 0.4918 for the zero sideslip and nonzero sideslip cases, respectively.

The grid shown in Fig. 5 is used. It consists of two layers. The inner layer is $5 \times 97 \times 577$, and the outer layer is $5 \times 97 \times 385$ along the longitudinal, radial, and circumferential directions, respectively.

A. No-Sideslip Case

The flow code is first run in its steady-state mode, starting with a uniform stream. Figure 8 shows the contours of the longitudinal velocity component in various crossflow planes of the converged solution, and Fig. 9 plots the pressure contours in one particular crossflow plane. It is clear that the computed flowfield is symmetric with respect to the incidence plane ($y = 0$), confirming our analytical prediction of the existence of stationary symmetric vortex pairs over a delta wing. The right and left vortex cores are located at $x/s = 0.5439$ and $y/s = \pm 0.7129$, respectively.

The stability of the stationary symmetric vortex pair is then tested by introducing small asymmetric perturbations to the initial symmetric solution and switching the code to run in time-accurate mode. The small asymmetric perturbation A given by Eq. (4) is provided by blowing and suction on the right and left sides of the wing, respectively, over a short period of time, as shown by the antisymmetric arrows of V_j in Fig. 9.

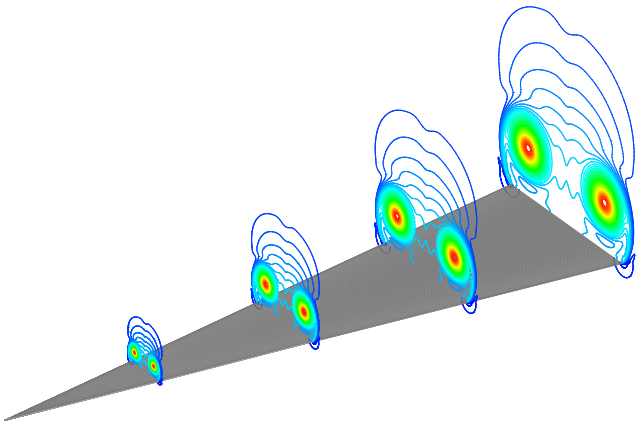

Fig. 8 Contours of the longitudinal velocity component in crossflow planes of a flat-plate delta wing; $\epsilon = 8$ deg, $\alpha = 28$ deg, and $\beta = 0$ deg.

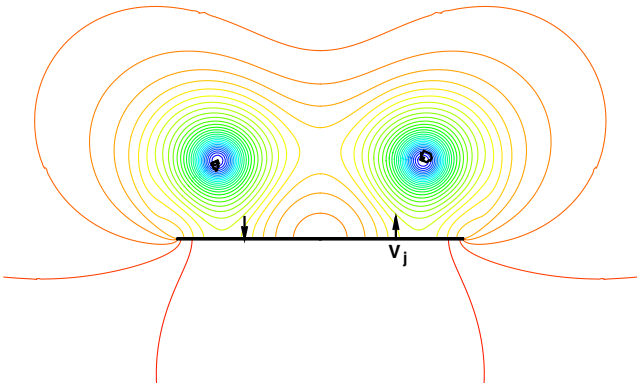

Fig. 9 Pressure contours in a crossflow plane and trajectories of the vortex cores after perturbation A is applied to the symmetric stationary vortex solution over a flat-plate delta wing; $\epsilon = 8$ deg, $\alpha = 28$ deg, and $\beta = 0$ deg.

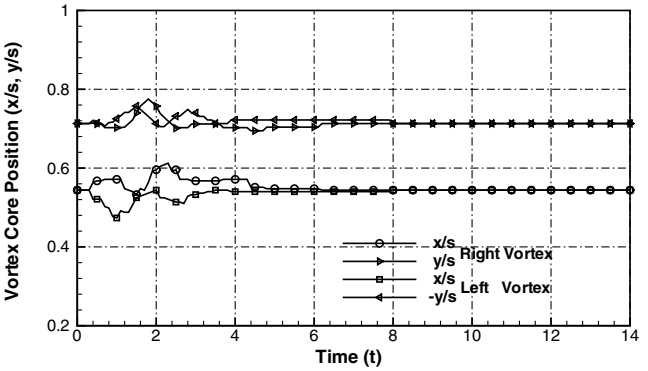

Fig. 10 Vortex-core position vs time after perturbation A is applied to the symmetric stationary vortex solution for a flat-plate delta wing; $\epsilon = 8$ deg, $\alpha = 28$ deg, and $\beta = 0$ deg.

On introducing the preceding perturbations to the original stationary symmetric vortex flowfield, the flow code is switched to running in time-accurate mode. The evolution of the vortex-core positions x/s and y/s captured by the computation is plotted in Fig. 10. The corresponding loci of the vortex cores are drawn by the solid lines overlapped on top of the pressure contours in a crossflow plane, as shown in Fig. 9. After initial deviations from their original stationary positions because of the flow perturbations, the two vortices gradually return to their original positions, indicating that the symmetric vortex pair is stable. This agrees fully with our analytical predictions shown in Fig. 6.

B. Sideslip Case

The flight condition that we consider for the nonzero sideslip case has a 13-deg yawing angle and 28-deg angle of attack, corresponding to a Sychev parameter $K = 3.7833$ and a sideslip similarity parameter $K_S = 0.4918$. The eigenvalues predicted by the theory and shown in Fig. 7 indicate that the asymmetric vortex pair remains stable for all values of K. Computations are performed for this case again by running the Euler code in its steady-state mode first in a similar fashion and on the same grid as in the zero sideslip case. Figure 11 shows the contours of the constant longitudinal velocity component in various crossflow planes of the steady-state solution. Figure 12 gives the pressure contours over one crossflow plane to show the vortex positions. The windward vortex core is at $x/s = 0.5132$ and $y/s = -0.5431$. The leeward vortex core is at $x/s = 0.8892$ and $y/s = 1.0439$. Relative to the no-sideslip case, the windward vortex moves inboard and remains nearly the same distance above the upper surface of the wing, whereas the leeward vortex moves outboard and upward from the wing for this nonzero sideslip case. This agrees with the analytical predictions in [20].

As in the zero sideslip case, perturbation to the preceding converged stationary asymmetric solution is introduced and the

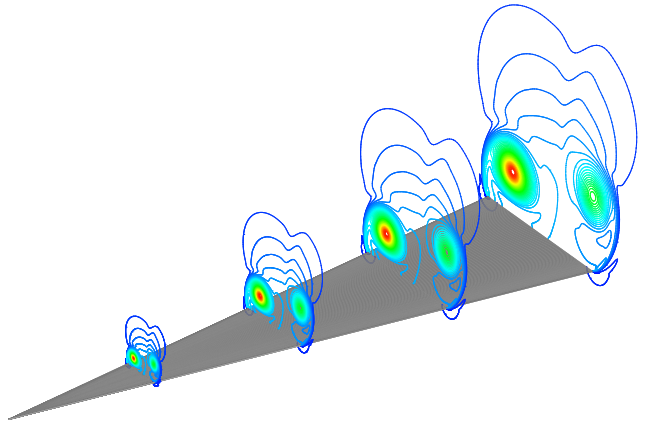

Fig. 11 Contours of the longitudinal velocity component in crossflow planes of a flat-plate delta wing; $\epsilon = 8$ deg, $\alpha = 28$ deg, and $\beta = 13$ deg.

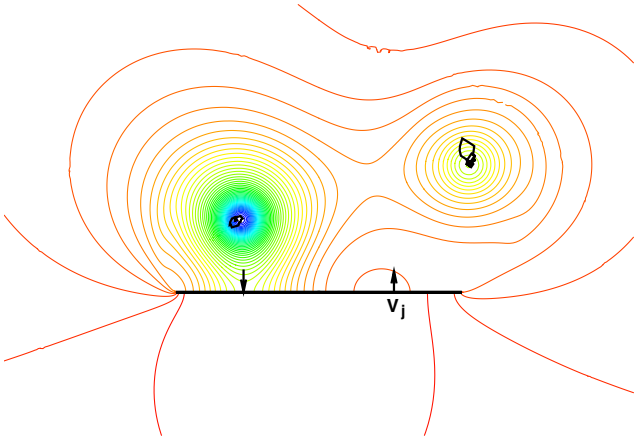

Fig. 12 Pressure contours in a crossflow plane and trajectories of the vortex cores after perturbation A is applied to the asymmetric stationary vortex solution over a flat-plate delta wing; $\epsilon = 8$ deg, $\alpha = 28$ deg, and $\beta = 13$ deg.

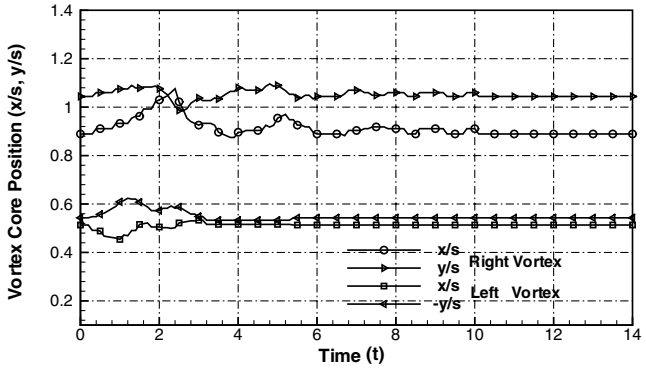

Fig. 13 Vortex-core position vs time after perturbation A is applied to the asymmetric stationary vortex solution for a flat-plate delta wing with sideslip, $\epsilon = 8$ deg, $\alpha = 28$ deg, and $\beta = 13$ deg.

computation is switched to the time-accurate mode to follow the motion of the vortices. The same perturbation A as in the zero sideslip case is used. Figure 12 plots the loci of the vortex centers after the perturbation is introduced on top of the pressure contours of the initial stationary asymmetric solution. Figure 13 shows the time history of the dimensionless coordinates of the vortex centers. Clearly, the two vortices return to their original undisturbed positions after initially wandering about for some time because of the disturbances. This again confirms the analytical prediction that the asymmetric vortex pair is stable. Furthermore, the theory predicts that the leeward (right) vortex is less stable compared with the windward (left) vortex, because the maximum real part of the eigenvalues for the leeward vortex is closer to zero than that for the windward vortex (see Fig. 7). The computed time history of the vortex locations shown in Fig. 13 indicates that the excursion of the leeward vortex persists longer than that of the windward vortex before both of them return to their stationary locations, in agreement with the analytical prediction.

V. Wing–Body Combination of a Flat-Plate Delta Wing and a Circular-Cone Body

A number of wing–body combinations are studied in [21] by the present analytical method. A typical case is considered in this paper. The flow over a combination of a flat-plate delta wing and a circular-cone body with a body-width-to-wing-span ratio $\gamma = 0.7$ is examined under the condition of no sideslip. The delta wing has an semiapex angle of $\epsilon = 8$ deg. No stationary asymmetric vortex pair is found in the analytical studies [21] at low angles of attack when the Sychev similarity parameter $K \leq 2.5$. At higher K, both symmetric and asymmetric stationary vortex pairs exist. As K is increased, both stationary symmetric and asymmetric vortex pairs move upward and outboard. The movement of the lower vortex of the asymmetric vortex pair is much smaller and that of the upper vortex is much greater compared with the movements of the symmetric vortices.

Figures 14 and 15 show the maximum real part of the eigenvalues for the stability of the symmetric and asymmetric vortex pairs, respectively, under small symmetric and antisymmetric perturbations. The stationary symmetric vortex pair is stable when $K \leq 2.58$ and unstable otherwise. The asymmetric vortex pair is only stable when $K \geq 2.62$ (the upper vortex is the least stable and becomes unstable for $K < 2.62$.) Therefore, we presume that a stable symmetric vortex pair at low angles of attack transits into a stable asymmetric pair as the angle of attack is increased beyond approximately $K = 2.58$–2.62.

Computations are performed for this wing–body combination at three sample angles of attack: $\alpha = 18$, 28, and 30 deg, corresponding to $K = 2.3119$, 3.7833, and 4.1080, respectively. According to the analytical predictions shown in Figs. 14 and 15, the stationary symmetric vortex pair is stable for the first case when $K = 2.3119$. For the latter two cases, the stationary symmetric vortex pair is not stable. Instead, the system favors a stable asymmetric vortex pair. It is attempted here to compute the flow for the three cases and compare the numerical results with the analytical predictions.

Again, the grid type shown in Fig. 5 is used. This time, however, the grid consists of three layers: the inner layer has $5 \times 177 \times 581$ grid points in eight blocks, the intermediate layer has $5 \times 49 \times 385$ grid points in two blocks, and the outer layer has $5 \times 49 \times 257$ grid

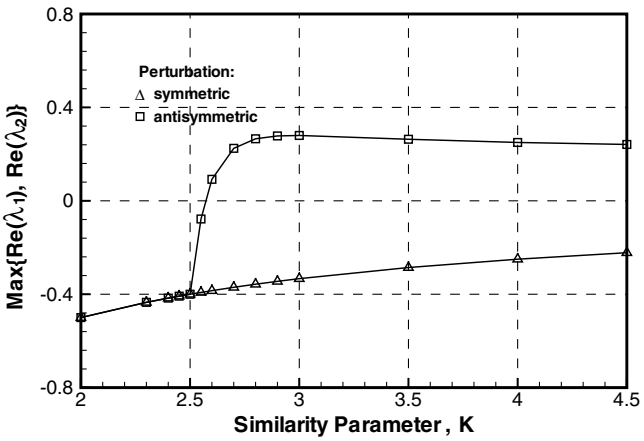

Fig. 14 Maximum real part of eigenvalues of symmetric vortex pairs over a wing–body combination of a flat-plate delta wing and a circular-cone body vs K; $\gamma = 0.7$ and $K_S = 0$.

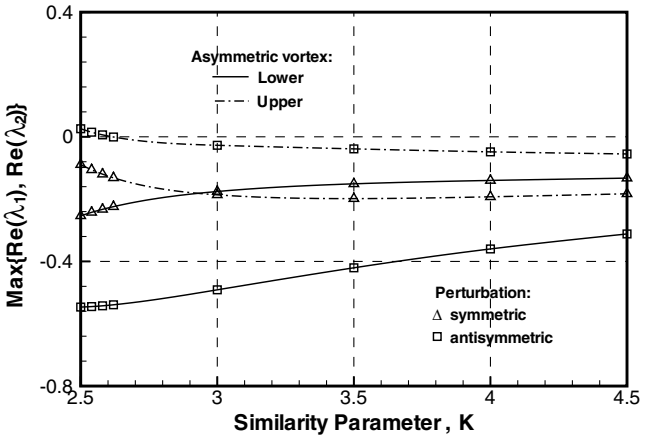

Fig. 15 Maximum real part of eigenvalues of asymmetric vortex pairs over a wing–body combination of a flat-plate delta wing and a circular-cone body vs K; $\gamma = 0.7$ and $K_S = 0$.

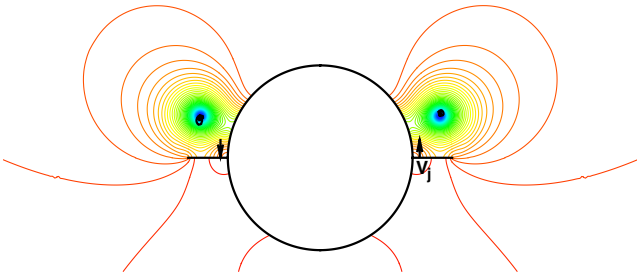

Fig. 16 Pressure contours in a crossflow plane and trajectories of the vortex cores after perturbation B is applied to the symmetric stationary vortex solution over a wing–body combination of a flat-plate delta wing and a circular-cone body; $\epsilon = 8$ deg, $\gamma = 0.7$, $\alpha = 18$ deg, and $\beta = 0$ deg.

points in two blocks. The inner layer has two sublayers, each of which has four blocks. The upper half of the inner sublayer has $5 \times 81 \times 387$ grid points, and the upper half of the outer sublayer has $5 \times 97 \times 387$ grid points. Computations of the three sample cases are reported next, in order.

A. Stable Symmetric Vortex Case, $\alpha = 18$ deg ($K = 2.3119$)

Figure 16 shows the pressure contours of the converged steady-state solution in a crossflow plane for this case. The flowfield is symmetric with respect to the incidence plane. The vortex cores are located at $x/s = 0.3146$ and $y/s = \pm 0.9078$.

The symmetric solution thus obtained represents a stationary vortex configuration. To investigate the stability of the stationary vortex flow, perturbation B is applied to the preceding converged steady-state solution. The time history of the computed dimensionless x and y coordinates of the two vortex cores are recorded in Fig. 17. The tiny closed loops that pass through the stationary vortex centers shown in Fig. 16 represent the computed trajectories of the two vortices. It is seen that the disturbed flow returns to the original symmetric configuration, confirming the analytical prediction shown in Fig. 14 that the stationary symmetric vortex flow over the wing–body combination at $\alpha = 18$ deg ($K = 2.3119$) is stable under small perturbations.

B. Bistable Asymmetric Vortex Case, $\alpha = 28$ deg ($K = 3.7833$)

Similar to the preceding study, a stationary vortex flow is searched for by running the Euler solver in its steady mode. For this case, however, the theory predicts two possible stationary solutions [21]: one symmetric and one asymmetric. The Euler solver used in the present study is based on an explicit central-differencing-type finite volume scheme. The algorithm is intrinsically symmetric. With a uniform freestream flow as the initial solution, the resulting steady-state solution is found to be perfectly symmetric similar to that shown in Fig. 16. The two vortex cores are symmetrically located at $x/s = 0.5741$ and $y/s = \pm 0.9174$. Clearly, this solution represents a stationary symmetric vortex flow, which is subjected to a stability examination.

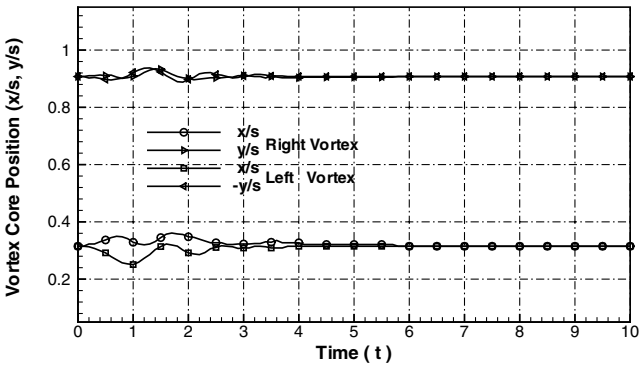

Fig. 17 Vortex-core position vs time after perturbation B is applied to the symmetric stationary vortex solution over a wing–body combination of a flat-plate delta wing and a circular-cone body; $\epsilon = 8$ deg, $\gamma = 0.7$, $\alpha = 28$ deg, and $\beta = 0$ deg.

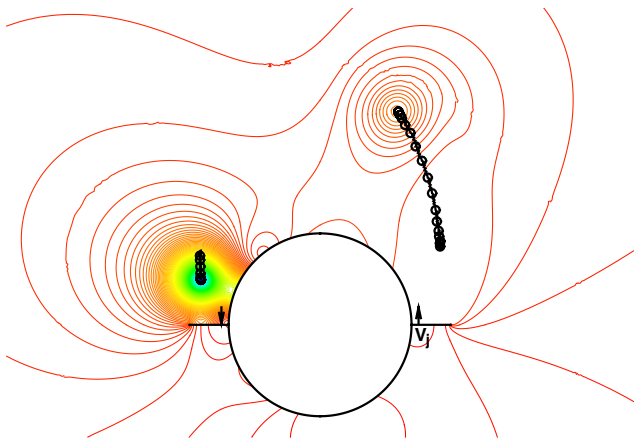

Fig. 18 Pressure contours in a crossflow plane and trajectories of the vortex cores after perturbation B is applied to the symmetric stationary vortex solution over a wing–body combination of a flat-plate delta wing and a circular-cone body; $\epsilon = 8$ deg, $\gamma = 0.7$, $\alpha = 28$ deg, and $\beta = 0$ deg.

Perturbation B of Eq. (4) is introduced to the preceding symmetric stationary vortex configurations. As before, the Euler solver is run in time-accurate mode upon the introduction of the preceding disturbance. Unlike in the previous case, however, the disturbed flow does not return to its starting stationary configuration, even after the initial disturbance has long disappeared. Instead, it wanders farther and farther away until it reaches a new steady-state solution, shown in Fig. 18, in which the two lines with circles mark the trajectories of the two vortex centers and the contours are constant pressure lines of the newly obtained steady-state solution at the end of the time-accurate computation. Figure 19 shows the vortex-core positions x/s and y/s vs the nondimensional time t. The new steady-state solution is highly asymmetric. The left vortex moved a small distance down toward the wing surface, whereas the right vortex wandered significantly farther above and to the left compared with the original symmetric solution. The left (lower) vortex core is at $x/s = 0.3448$ and $y/s = -0.9127$. The right (upper) vortex core is at $x/s = 1.6320$ and $y/s = 0.5992$. Notice that the disturbances are only imposed for a short time duration ($0 < t < 1$), whereas the computation is continued without any externally imposed disturbance or asymmetry from $t = 1$ until $t = 64$ (see the abscissa of Fig. 19.) This can only be explained by the fact that the initial symmetric vortex solution (obtained under a very stringent convergence criterion) is not a stable configuration, and the new asymmetric solution must also be a possible stationary vortex configuration, which is in complete agreement with the analytical prediction.

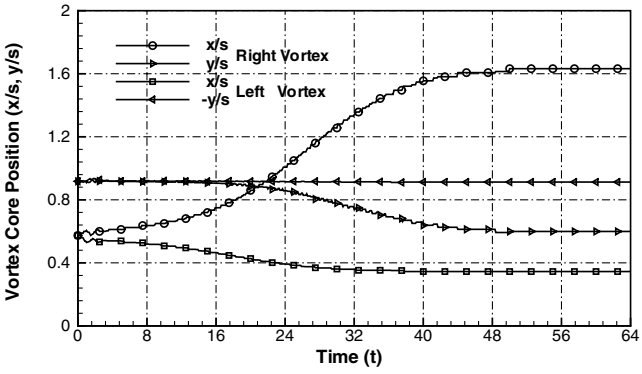

Fig. 19 Vortex-core position vs time after perturbation B is applied to the symmetric stationary vortex solution over a wing–body combination of a flat-plate delta wing and a circular-cone body; $\epsilon = 8$ deg, $\gamma = 0.7$, $\alpha = 28$ deg, and $\beta = 0$ deg.

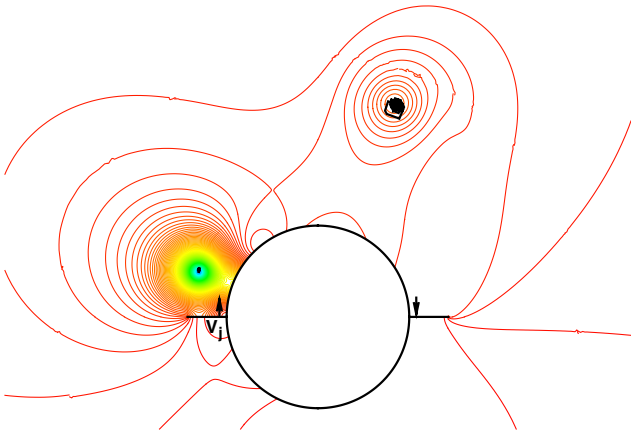

Fig. 20 Pressure contours in a crossflow plane of the asymmetric solution after application of perturbation *B* with reversed suction and blowing to the stationary asymmetric solution over a wing–body combination of a flat-plate delta wing and a circular-cone body; $\epsilon = 8$ deg, $\gamma = 0.7$, $\alpha = 28$ deg, and $\beta = 0$ deg; and trajectories of the perturbed vortex core.

Although the preceding computations demonstrate the existence of a stationary asymmetric vortex configuration in addition to the symmetric configuration for this angle-of-attack condition, it remains to be seen whether this asymmetric vortex pair is stable under small perturbations. To do this, time is reset to zero for the time-accurate Euler computations to continue with the new stationary asymmetric solution as the initial condition. Perturbation *B* is imposed for the initial unit time period ($0 < t < 1$). Just for variety, to demonstrate independence of initial perturbations, we present results with the suction and blowing directions exchanged. The new directions are shown by the two arrows of V_j in Fig. 20. The computed vortex-core positions vs time *t* are shown in Fig. 21. It is seen that the solution goes back to the initial asymmetric solution. The trajectories of the vortices during the flow evolution are shown by the solid lines around the vortex centers in Fig. 20. Although the excursions of the vortices last longer time periods (especially for the higher vortex) compared with the stable symmetric vortices considered in the previous subsection, both vortices return to their original locations, confirming our analytical prediction that the stationary asymmetric vortex pair for this angle of attack ($\alpha = 28$ deg and $K = 3.7833$) is stable under small perturbations. The computational finding that the computed disturbance of the upper vortex lasts longer than that for the lower vortex is again in agreement with the analytical prediction shown in Fig. 15 that the maximum real part of the eigenvalues for the upper vortex is closer to zero than that for the lower vortex.

Another question is whether the stationary asymmetric solution already obtained depends on the specific initial perturbations.

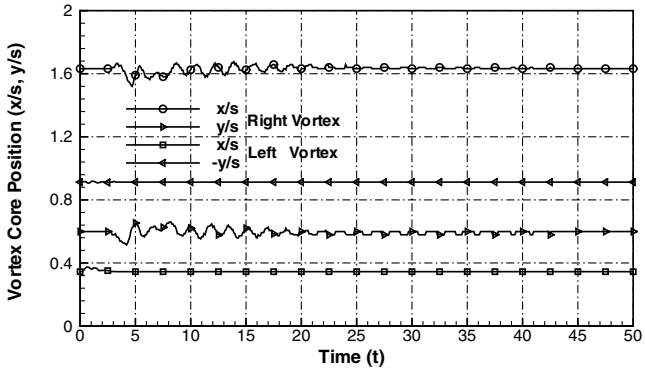

Fig. 21 Vortex-core position vs time after application of perturbation *B* with reversed suction and blowing to the stationary asymmetric solution over a wing–body combination of a flat-plate delta wing and a circular-cone body; $\epsilon = 8$ deg, $\gamma = 0.7$, $\alpha = 28$ deg, and $\beta = 0$ deg.

Computations have shown that the solutions always converge to one of two asymmetric configurations that are mirror images of each other. As an example, perturbation *C* is applied to the converged symmetric solution. Perturbation *C* is different from perturbation *B* in that it has the suction and blowing locations interchanged with lower strength and moved closer to the wing tips. The same time-accurate computations are performed as before. Again, the initial converged solution breaks away from symmetry under the initial (short time) asymmetric disturbance. This time, because of the reversed directions of the suction and blowing, the left vortex moves up and to the right, whereas the right vortex moves down. The final solution converges to an exact mirror image of the solution shown in Fig. 18 obtained by using perturbation *B*. Only one stationary symmetric solution and one stationary asymmetric solution are found analytically for this case, except for the mirror image of the asymmetric solution [21]. Thus, the computation and the theory agree that the only stable solutions for this case are the asymmetric vortex configuration shown in Fig. 18 and its mirror image.

Such bistable states are observed in wind-tunnel tests for slender pointed bodies at high angles of attack. For example, Zilliac et al. [6] measured the overall side force of a 3.5-caliber ogive-cylinder body of revolution using a six-component strain gauge balance at $Re = 3 \times 10^4$. The overall side-force coefficient against roll angles is a square-wave curve for 50 deg $< \alpha <$ 60 deg or, equivalently, $4 < K < 6$ if a cone is used to approximate the nose portion of the ogive-cylinder body. The asymmetry has only two stable, or bistable, states. The side-force coefficient switches abruptly from the constant positive value to the constant negative value of the same magnitude or vice versa over the whole range of roll angle, and no intermediate side-force coefficient is found.

C. Neutrally Stable Asymmetric Vortex Case, $\alpha = 30$ deg ($K = 4.1081$)

The steady-state solution for this case is obtained in Fig. 22. The solution is symmetric with the vortex cores located at $x/s = 0.6498$ and $y/s = \pm 0.9138$. The vortex cores are higher in position than those for the lower *K* values. They now almost clear the height of the centerbody ($x/s = 0.7$), potentially increasing the interaction between themselves.

As in the previous case, the theory predicts that this symmetric vortex flow is not stable, whereas an asymmetric vortex configuration is stable. Upon introduction of perturbation *B* to the computed symmetric solution, the time-accurate computation captures the evolution of the flow to approach a stationary asymmetric solution, shown in Fig. 23. The left vortex moves downward to reach $x/s = 0.3529$ and $y/s = -0.9144$. The right vortex moves up and to the left to reach $x/s = 1.8610$ and $y/s = 0.5320$. Compared with the previous case at a lower angle of attack, the upper vortex in this case is lifted to a higher position and is weakened and dispersed (not as concentrated).

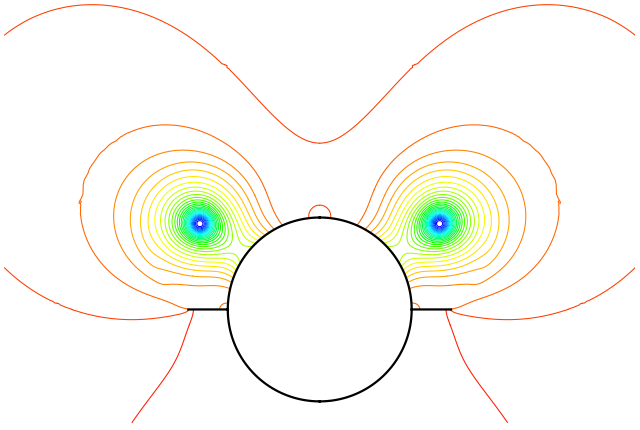

Fig. 22 Pressure contours in a crossflow plane over a wing–body combination of a flat-plate delta wing and a circular-cone body; $\epsilon = 8$ deg, $\gamma = 0.7$, $\alpha = 30$ deg, and $\beta = 0$ deg.

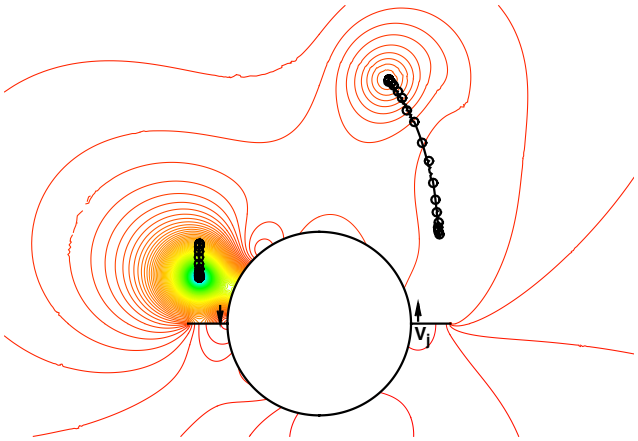

Fig. 23 Pressure contours in a crossflow plane and trajectories of the vortex cores after application of perturbation *B* to the symmetric solution over a wing–body combination of a flat-plate delta wing and a circular-cone body; $\epsilon = 8$ deg, $\gamma = 0.7$, $\alpha = 30$ deg, and $\beta = 0$ deg.

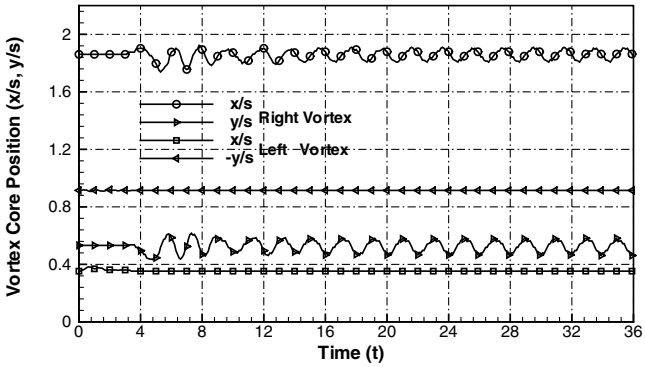

Fig. 24 Vortex-core position vs time after application of perturbation *B* with reversed suction and blowing to the asymmetric solution over a wing–body combination of a flat-plate delta wing and a circular-cone body; $\epsilon = 8$ deg, $\gamma = 0.7$, $\alpha = 30$ deg, and $\beta = 0$ deg.

To check the stability of the stationary asymmetric vortex pair, perturbation *B* (with reversed directions of suction and blowing) is introduced and the time-accurate computation is restarted with the stationary asymmetric solution as the initial condition. Figure 24 shows the time history of the coordinates of the vortex centers. The disturbances experienced by the left (lower) vortex are relatively small. This vortex tends to cling tight to the wing and body and quickly return to its stationary position. On the other hand, the right (upper) vortex reaches a cyclic motion, circling around its original stationary position with a small radius of $0.05s$, indicating a neutrally stable state rather than a strictly stable state as predicted by the theory. This aspect of the result is not in complete agreement with the analytical prediction. The Euler solutions, as exemplified in Figs. 8 and 11, capture the vortex sheets that roll up from the sharp leading edges of the wing. These side vortex sheets, which are much weaker than the concentrated line vortices when they are not too far away from the body surface, are neglected in the theoretical model. However, for this asymmetric case, the extent of the side vortex sheet for the higher-positioned vortex becomes significant compared with the weakened concentrated line vortex.

An advantage of the theory is that it allows us to obtain continuous stability curves, as shown in Figs. 6, 7, 14, and 15. Computations, however, are discrete by definition and therefore cannot be exhaustive. With limited computational resources, we can (and probably need only to) check on a few typical points. No attempt is made in the present study to compute near or to locate the critical point at which the vortices change from being stable to unstable. This is because, by definition, disturbances grow or decay very slowly near the critical point; therefore, the computational time will be excessively long to demonstrate such a condition. Furthermore, an exact quantitative agreement on the critical point between theory and computation is not expected because of the neglected vortex sheets in the theory already discussed and the small amount of numerical dissipation that exists in any numerical computation using finite grid sizes.

VI. Conclusions

Analytical and computational methods are presented for the study of the stability of vortices over slender conical bodies at high angles of attack. The analytical method is based on a general stability theory and a slender conical-flow model. The computational method is based on a three-dimensional, parallel, multiblock, multigrid, finite volume method for the Euler equations. The method uses central-differencing with a fourth-order artificial dissipation. The code preserves symmetry and is run in double-precision (64-bit arithmetic) on very fine grids with stringent convergence criteria. Stationary vortex configurations are first captured by running the Euler code in its steady-state mode. After a stationary vortex-flow configuration is obtained, an antisymmetric perturbation consisting of suction and blowing is introduced to the flow and the Euler code is run in time-accurate mode to determine if the flow will return to its original undisturbed condition or evolve into a different steady or unsteady solution after withdrawal of the initial disturbances. The former indicates stability, whereas the latter indicates instability of the flow to the applied perturbation.

The computational approach is applied to wing-alone and wing–body-combination configurations in parallel with the analytical method. The first configuration is the flow over a flat-plate delta wing with and without sideslip. With zero sideslip, the theory predicts that one stationary symmetric vortex pair exists for each angle of attack and that all such vortices are stable. In addition, there are no asymmetric stationary vortices at zero sideslip. With sideslip, the stationary vortex pair becomes asymmetric, but it is also stable. Computations performed for a flat-plate delta wing of 82-deg sweep angle and at typical flight conditions confirm all of the preceding analytical predictions. In addition, they also reveal the relative levels of stability of the two vortices, in complete agreement with the analytically predicted magnitudes of the eigenvalues.

The second configuration is a combination of a flat-plate delta wing of 82-deg sweep angle and a circular-cone body of a radius equal to 70% of the wing semispan at zero sideslip. Three sample angles of attack ($\alpha = 18$, 28, and 30 deg) are considered in the computations. Both the theory and the computation show that the vortices over this wing–body configuration at the low angle of attack are symmetric and stable, but become bistable at the higher angles of attack, a condition in which the vortices take only two stable (or neutrally stable) asymmetric configurations that are mirror images of each other. This is in agreement with known experimental observations.

The computations of the finite but judiciously chosen cases agree well with the theory and thus confirm the validity of the stability analysis. Together, they support the conclusion that a global-type inviscid hydrodynamic instability of the vortex configuration provides a mechanism for the breaking of symmetry of the vortex flow over slender conical bodies at high angles of attack.

References

[1] Hunt, B. L., "Asymmetric Vortex Forces and Wakes on Slender Bodies," AIAA Paper 1982-1336, Aug. 1982.

[2] Ericsson, L., and Reding, J., "Asymmetric Flow Separation and Vortex Shedding on Bodies of Revolution," *Tactical Missile Aerodynamics: General Topics, Progress in Astronautics and Aeronautics*, edited by M. Hemsh, Vol. 141, AIAA, New York, 1992, pp. 391–452.

[3] Champigny, P., "Side Forces at High Angles of Attack: Why, When, How?" *La Recherche Aerospatiale : Bulletin Bimestriel de l'Office National d'Etudes et de Recherches Aerospatiales*, No. 4, 1994, pp. 269–282.

[4] Dexter, P., and Hunt, B. L., "The Effects of Roll Angle on the Flow over a Slender Body of Revolution at High Angles of Attack," AIAA Paper 1981-0358, 1981.

[5] Lamont, P. J., "Pressures Around an Inclined Ogive Cylinder with Laminar, Transitional, or Turbulent Separation," *AIAA Journal*, Vol. 20, No. 11, Nov. 1982, pp. 1492–1499.
[6] Zilliac, G. G., Degani, D., and Tobak, M., "Asymmetric Vortices on a Slender Body of Revolution," *AIAA Journal*, Vol. 29, No. 5, May 1991, pp. 667–675.
[7] Degani, D., "Effect of Geometrical Disturbance on Vortex Asymmetry," *AIAA Journal*, Vol. 29, No. 4, Apr. 1991, pp. 560–566.
[8] Degani, D., "Instabilities of Flows over Bodies at Large Incidence," *AIAA Journal*, Vol. 30, No. 1, Jan. 1992, pp. 94–100.
[9] Levy, Y., Hesselink, L., and Degani, D., "Systematic Study of the Correlation Between Geometrical Disturbances and Flow Asymmetries," *AIAA Journal*, Vol. 34, No. 4, Apr. 1996, pp. 772–777.
[10] Hartwich, P. M., Hall, R. M., and Hemsch, M. J., "Navier–Stokes Computations of Vortex Asymmetries Controlled by Small Surface Imperfections," *Journal of Spacecraft and Rockets*, Vol. 28, No. 2, Mar.–Apr. 1991, pp. 258–264.
[11] Bryson, A., "Symmetrical Vortex Separation on Circular Cylinders and Cones," *Journal of Applied Mechanics*, Vol. 26, Dec. 1959, pp. 643–648.
[12] Dyer, D. E., Fiddes, S. P., and Smith, J. H. B., "Asymmetric Vortex Formation from Cones at Incidence—A Simple Inviscid Model," *Aeronautical Quarterly*, Vol. 33, Pt. 4, Nov. 1982, pp. 293–312.
[13] Pidd, M., and Smith, J. H. B., "Asymmetric Vortex Flow over Circular Cones," *Vortex Flow Aerodynamics*, AGARD AGARD-CP-494, Neuilly sur Seine, France, July 1991, pp. 18–1–11.
[14] Degani, D., and Tobak, M., "Experimental Study of Controlled Tip Disturbance Effect on Flow Asymmetry," *Physics of Fluids A*, Vol. 4, No. 12, 1992, pp. 2825–2832. doi:10.1063/1.858338
[15] Ng, T. T., and Malcolm, G. N., "Aerodynamic Control Using Forebody Blowing and Suction," AIAA Paper 91-0619, Jan. 1991.
[16] Bernhardt, J. E., and Williams, D. R., "The Effect of Reynolds Number on Vortex Asymmetry About Slender Bodies," *Physics of Fluids A*, Vol. 5, No. 2, 1993, pp. 291–293. doi:10.1063/1.858693
[17] Legendre, R., "Écoulement au Voisinage de la Pointe Avant d'une aile a Forte Fléche aux Incidences Moyennes," *Recherche Aéronautique*, No. 30, 1952, pp. 3–8.
[18] Huang, M. K., and Chow, C. Y., "Stability of Leading-Edge Vortex Pair on a Slender Delta Wing," *AIAA Journal*, Vol. 34, No. 6, June 1996, pp. 1182–1187.
[19] Cai, J., Liu, F., and Luo, S., "Stability of Symmetric Vortices in Two-Dimensions and over Three-Dimensional Slender Conical Bodies," *Journal of Fluid Mechanics*, Vol. 480, No. 4, Apr. 2003, pp. 65–94. doi:10.1017/S0022112002003567
[20] Cai, J., Luo, S., and Liu, F., "Stability of Symmetric and Asymmetric Vortex Pairs over Slender Conical Wings and Bodies," *Physics of Fluids*, Vol. 16, No. 2, Feb. 2004, pp. 424–432. doi:10.1063/1.1637601
[21] Cai, J., Luo, S., and Liu, F., "Stability of Symmetric and Asymmetric Vortices over Slender Conical Wing–Body Combinations," *AIAA Journal*, Vol. 44, No. 7, July 2006, pp. 1601–1608.
[22] Cai, J., Tsai, H.-M., Luo, S., and Liu, F., "Study of Stability of Vortex Pairs over a slender Conical Body by Euler Computations," *Frontiers of Computational Fluid Dynamics 2006*, edited by D. A. Caughey and M. Hafez, World Scientific, Hackensack, NJ, Dec. 2005, pp. 297–323.
[23] Sychev, V., "Three-Dimensional Hypersonic Gas Flow Past Slender Bodies at High Angle of Attack," *Journal of Mathematics and Mechanics*, Vol. 24, Feb. 1960, pp. 296–306. doi:10.1016/0021-8928(60)90033-2
[24] Liu, F., and Jameson, A., "Multigrid Navier–Stokes Calculations for Three-Dimensional Cascades," *AIAA Journal*, Vol. 31, No. 10, Oct. 1993, pp. 1785–1791.
[25] Liu, F., and Zheng, X., "A Strongly-Coupled Time-Marching Method for Solving the Navier–Stokes and k-ω Turbulence Model Equations with Multigrid," *Journal of Computational Physics*, Vol. 128, No. 2, 1996, pp. 289–300. doi:10.1006/jcph.1996.0211
[26] Liu, F., and Ji, S., "Unsteady Flow Calculations with a Multigrid Navier–Stokes Method," *AIAA Journal*, Vol. 34, No. 10, Oct. 1996, pp. 2047–2053.
[27] Sadeghi, M., Yang, S., Liu, F., and Tsai, H.-M., "Parallel Computation of Wing Flutter with a Coupled Navier–Stokes/CSD Method," AIAA Paper 2003-1347, Jan. 2003.
[28] Cai, J., Tsai, H.-M., and Liu, F., "An Overset Grid Solver for Viscous Computations with Multigrid and Parallel Computing," *Computers and Fluids*, Vol. 35, No. 10, 2006, pp. 1290–1301. doi:10.1016/j.compfluid.2005.02.006
[29] Cummings, R., Forsythe, J., Morton, S., and Squires, K., "Computational Challenges in High Angle of Attack Flow Prediction," *Progress in Aerospace Sciences*, Vol. 39, No. 5, May 2003, pp. 369–384. doi:10.1016/S0376-0421(03)00041-1
[30] Levy, Y., Hesselink, L., and Degani, D., "Anomalous Asymmetries in Flow Generated by Algorithms That Fail to Conserve Symmetry," *AIAA Journal*, Vol. 33, No. 6, June 1995, pp. 999–1007.
[31] Hartwich, P. M., "Symmetry Breaking in Vortical Flows Over Cones—Theory and Numerical Experiments," *AIAA Journal*, Vol. 32, No. 5, May 1994, pp. 1013–1020.
[32] Thomas, J. L., "Reynolds Number Effects on Supersonic Asymmetrical Flows over a Cone," *Journal of Aircraft*, Vol. 30, No. 4, July–Aug. 1993, pp. 488–495.
[33] Van Dyke, M., *An Album of Fluid Motion*, Parabolic Press, Stanford, CA, 1982, p. 54.
[34] Thomas, J., Kirst, S., and Anderson, W., "Navier–Stokes Computations of Vortical Flows over Low-Aspect-Ratio Wings," *AIAA Journal*, Vol. 28, No. 2, Feb. 1990, pp. 205–212.
[35] Rizzi, A., "Euler Solutions of Transonic Vortex Flows Around the Dillner Wing," *Journal of Aircraft*, Vol. 22, No. 4, Apr. 1985, pp. 325–328.
[36] Siclari, M., and Marconi, F., "Computation of Navier–Stokes Solutions Exhibiting Asymmetric Vortices," *AIAA Journal*, Vol. 29, No. 1, Jan. 1991, pp. 32–42.

A. Plotkin
Associate Editor